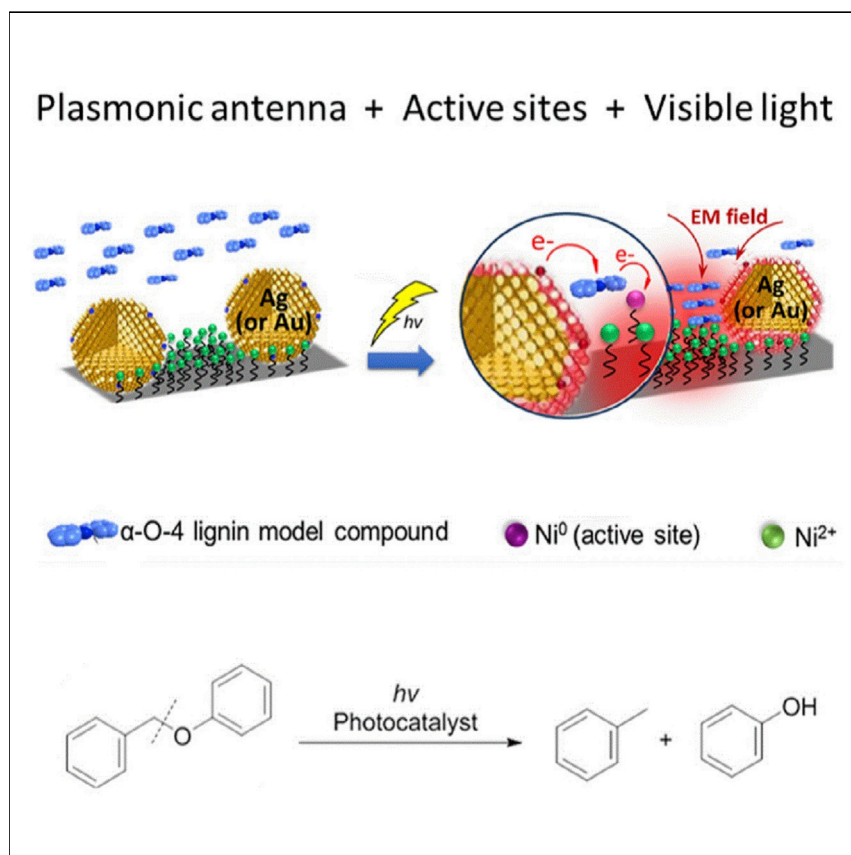


Article

Promoting Ni(II) Catalysis with Plasmonic Antennas



Plasmonic metal NPs such as Au and Ag are proven to channel visible-light photon energy to nearby metal complexes effectively and allow the conventional metal cationic catalysts to work at moderate temperatures under light irradiation. A key finding is that reactant molecules can be significantly concentrated at the active sites simply by light and thus increase the chance of activation. The merging of plasmonic antenna and metal cationic catalysis will be an inspiring strategy for designing efficient photocatalytic systems.

Pengfei Han, Tana Tana, Qi Xiao, Sarina Sarina, Eric R. Waclawik, Daniel E. Gómez, Huaiyong Zhu

s.sarina@qut.edu.au (S.S.)
hy.zhu@qut.edu.au (H.Z.)

HIGHLIGHTS

Plasmonic antenna enhances the catalytic activity of Ni²⁺ complexes by light

Reactants are concentrated at the catalyst surface by plasmonic electromagnetic field

Hot electrons are transferred via a molecular bridge of the benzyl ring of the reactants

Enhanced chemisorption by irradiation significantly increases the reaction rate



Article

Promoting Ni(II) Catalysis with Plasmonic Antennas

Pengfei Han,^{1,2} Tana Tana,² Qi Xiao,³ Sarina Sarina,^{2,5,*} Eric R. Waclawik,² Daniel E. Gómez,^{3,4} and Huaiyong Zhu^{2,*}

SUMMARY

Plasmonic catalysis has drawn significant interest recently, as the catalysis can be driven by visible light. Here, we show a new tactic to apply low-flux visible-light irradiation on plasmonic metal nanoparticles (NPs) to initiate catalysis with surface-bound transition-metal complexes under mild conditions. Ni²⁺ complexes (as catalytic reaction sites) and Au or Ag NPs were immobilized on γ -Al₂O₃ nanofibers to produce plasmonic-antenna-promoted catalysts. The light irradiation on Au or Ag NPs enhanced photocatalytic activity of the Ni²⁺ complexes for reductive cleavage of C–O bond by 18-fold or 17-fold, respectively. The intense electromagnetic near-fields of the plasmonic metal NPs significantly increased the chemisorption of the reactant to the Ni²⁺ active sites. The light-excited hot electrons transfer via a molecular bridge of the aromatic ring of the reactants. The light-enhanced chemisorption plays a key role in this photocatalyst's structure that comprises a plasmonic antenna and catalytically active metal complex sites.

INTRODUCTION

Direct photocatalysis using plasmonic metal (gold, silver, copper, or aluminum) nanoparticles (NPs) under visible-light irradiation, also called plasmonic catalysis, has drawn significant interest in the last decade.^{1–13} When plasmonic metal NPs are illuminated, they can efficiently absorb visible light due to the excitation of localized surface plasmon resonance (LSPR), where the conduction electrons of the NPs collectively oscillate with the electromagnetic (EM) field of incident light.¹⁴ The plasmon-resonant excitation generates energetic hot electrons that can trigger chemical reactions of a reactant adsorbed on the plasmonic NPs, under mild reaction conditions.^{1–7,12,13} However, only a limited number of the transformations can be directly catalyzed by NPs of plasmonic metals, especially when compared to the range of transformations accessible with transition-metal complexes in homogeneous catalysis systems. For specific reactions, photocatalysts of alloy NPs of a plasmonic and a transition metal of inherent catalytic activity for specific reactions have been developed to expand the application of the plasmonic photocatalysis to a wider range of selective organic synthesis reactions.¹⁵

Transition-metal complexes are widely used for the homogeneous catalytic synthesis of many important organic compounds.^{16–19} Combining the optical function of plasmonic metal NPs with the inherent bond-forming or bond-breaking ability of transition-metal complexes may enable the transition-metal complexes to catalyze reactions with the light energy harvested by plasmonic metal NPs under mild conditions. With traditional catalysis reactions, intense thermal heating is often required to bridge reaction activation barriers and achieve sufficient catalytic efficiency.

The Bigger Picture

Plasmonic metal nanoparticles (NPs) absorb visible light intensely; this produces hot electrons on their surface and also generates localized electromagnetic fields near the surfaces. This property is successfully applied to enhance the catalytic performance of typical metal-cationic-catalyst-Ni²⁺ complexes by low-flux visible-light irradiation. Here, Ni²⁺ complexes are immobilized in close proximity to Au (or Ag) NPs, which serve as the light-harvesting antennas and trigger the activity of Ni²⁺ catalysts effectively for the C–O bond cleavage reaction by 17- to 18-fold enhancement. The intense electromagnetic near-fields of irradiated plasmonic NPs enable the reactant molecule to be significantly concentrated at active sites and play a key role in the photo-accelerated reaction rates. This research could inspire a new paradigm to modify the conventional metal cationic catalysis by visible light.



Figure 1. The Schematic Structure of the Photocatalyst

Ni^{2+} complexes and plasmonic metal NPs are immobilized on $\gamma\text{-Al}_2\text{O}_3$ nanofibers. The randomly oriented nanofibers form connected cages of irregular shapes. Right: the photocatalytic reaction investigated in the present study.

When plasmonic metal NPs are introduced as antennas to direct energy to the active reaction site, there may be no need for such intensive heating. This difference in the way catalysis is expected to prove beneficial for selective synthesis. In a combined system, the plasmonic NP surfaces do not act as catalytically active sites themselves; instead, the NPs facilitate chemical transformations via the transfer of energy and light-generated hot electrons to reactive transition-metal complex sites, as schematically illustrated in Figure 1. The adsorption and activation of reactants at the complex sites of the new catalysts are different from those on metal NP surface.

It is well known that the LSPR light absorption of plasmonic NPs can generate EM near-fields, with intensities much higher than that of the incident radiation.^{4,6–11} The plasmon field enhancement can significantly change the light-matter interaction in excitonic systems.^{14,20} For instance, the field intensity in a narrow junction between Ag NPs has been predicted to be 10^6 times that of the incident light alone.⁴ These narrow junctions between closely spaced NPs are the so-called hot spots.^{21,22} Whether the high intensity of EM fields at the hot spots can be utilized for catalysis by surface-bound active sites has not been investigated. We consider that the strong EM fields at hot spots may radically change the interaction between reactant and transition-metal complexes when the complexes are immobilized within the hot spots. A strong interaction may direct the energy of the incident light to the reaction site. Also, since the number density of plasmonic NPs is larger at hot spots than other regions in a sample, the number of hot electrons at hot spots is also predicted to be higher. These properties may facilitate a chemical transformation and thus improve the catalytic efficiency of the metal complexes.

Electron transfer may contribute to the catalysis process by changing the oxidation state of the transition metal complexes, a key mechanism that can promote catalysis of many reactions.²³ In a combined system, the transfer of energy and hot electrons is determined by energy alignment: the energy of photoexcited electrons have to be sufficiently high to be injected into the metal complex sites (via a medium) and change the metal oxidation state. The light harvested by plasmonic NP antennas promotes conduction electrons to energy levels above the Fermi level,^{4,12,14} and energy distribution of hot electrons depends on the energy of the incident photons and the light absorption mechanism of the plasmonic metal NPs.

¹College of Chemistry and Chemical Engineering, Hunan University, Changsha 410082, P.R. China

²School of Chemistry, Physics and Mechanical Engineering, Queensland University of Technology, Brisbane, QLD 4001, Australia

³CSIRO Manufacturing, Bayview Ave, Clayton, VIC 3168, Australia

⁴RMIT University, Melbourne, VIC 3000, Australia

⁵Lead Contact

*Correspondence: s.sarina@qut.edu.au (S.S.), hy.zhu@qut.edu.au (H.Z.)

<https://doi.org/10.1016/j.chempr.2019.07.022>

In addition to the intraband electron excitation in the plasmonic NPs due to the LSPR effect, interband excitation of $d \rightarrow sp$ transitions by visible light can generate electron-hole (e^-h^+) pairs in Au NPs, which can participate in a chemical reaction of adsorbate on the NP surface.²⁴ The interband excitation in NPs of non-plasmonic metals can also facilitate chemical reactions.²⁵ It is of great interest to know whether the interband excitation can promote catalytic performance of the metal complexes at a distance. Small Au NPs possess only weak LSPR absorption and the light absorption of the NPs exposed to short wavelengths (<450 nm) induces predominantly interband excitation.¹² This property of small Au NPs can therefore be used to investigate whether interband excitation can promote the catalysis even when the NP surfaces are not catalytically active sites themselves. Hence, the mechanisms of the systems with the plasmon-antenna-promoted catalysts will be different from those of the plasmonic metal NP catalysts and homogeneous metal complex catalysts. These features are of great interest from a fundamental research perspective.

To verify the efficacy of the proposed strategy of exploiting the antenna-effect of plasmonic metal NPs and to develop protocols for transition-metal-catalyzed reactions under mild conditions, we designed a structure as illustrated in Figure 1. In this structure, Ni^{2+} complexes and Ag or Au NPs are immobilized on $\gamma-Al_2O_3$ nanofibers. Immobilizing Ni^{2+} complexes to the $\gamma-Al_2O_3$ supports maintains the complexes at fixed locations relative to the metal NPs, allowing us to investigate the influence of the high intensity of EM near-fields and transfer of hot electrons from the metal NPs to Ni^{2+} ions. Such a structure can achieve stable photocatalytic performance and make the catalysts recyclable.

Ni^{2+} complexes have been extensively used as homogeneous catalysts.^{26–29} Nickel is a common, inexpensive transition metal and has been used to catalyze reductive cleavage of C–O bonds.^{30–35} This reaction was chosen as a model reaction because it is the essential reaction step for the production of high-value aromatic chemicals from biopolymer lignin.³⁶ Aryl ether C–O bonds are relatively unreactive; for example, the dissociation energy of the aryl ether C–O bonds in the α -O-4 linkage is 218 kJ mol⁻¹.³¹ So catalysts usually function at high temperatures and hydrogen pressures (>120°C and added hydrogen pressure),³⁷ inevitably yielding saturated hydrocarbons. To avoid undesired hydrogenolysis of aromatic rings and to achieve selective cleavage of the aryl ether C–O bonds, the reaction should ideally be conducted under mild reaction conditions (low temperature and pressure). Hence, the catalysts must be highly active and selective to the C–O bond. Cleavage of C–O bonds in aryl ethers with a photocatalyst [Ir(ppy)₂(dtbbpy)]PF₆ at room temperature was reported recently.³⁸ Although these types of organometallic homogeneous photocatalysts are efficient, they are generally expensive and their use requires costly recycling processes.

In the present study, photocatalysts with immobilized Ni^{2+} complexes and plasmonic metal NPs were applied to the hydrogenolysis of benzyl phenyl ether that has an α -O-4 linkage.³⁹ We demonstrate that by varying the metal NP loading on the alumina support, the number of the plasmonic hot spots could be substantially altered. The hot electrons generated by both interband excitation of small Au NPs and intraband excitation (via LSPR effect) of Ag NPs can promote the catalysis. A significant observation is evidence for a light-induced, enhanced chemisorption of the reactant molecules at the catalytic active Ni^{2+} sites. This is beneficial to the catalytic performance of the Ni^{2+} sites. We also find that transfer of the hot electrons from the plasmonic metal NPs to the Ni^{2+} complexes via a “bridge” of the aromatic ring of the reactant is essential to the performance of the photocatalysts.

RESULTS AND DISCUSSION

Photocatalyst Structure

The photocatalysts were prepared following the procedures shown in Figure S1. The prefix number of the sample name indicates the plasmonic metal content in weight percentage (wt %), and ASN (alumina-silane-NH₂) is the support of Al₂O₃ nanofibers grafted with a silane containing an amino group. The metal content in the catalysts was measured by inductively coupled plasma optical emission spectrometry (ICP-OES), confirming the contents of Ni and plasmonic metal (Table S1). For example, the 2.5Au-ASN-Ni²⁺ catalyst contains 2.5 wt % of Au NPs, and Ni²⁺ ions are immobilized on the ASN support.

The γ -Al₂O₃ nanofibers are ~5 nm thick and 100 nm long, which were sintered to form a highly porous framework of randomly oriented fibers.⁴⁰ The cage-like nanofiber configuration (see Figure 1) could confine the NPs formed within the structure and allow reactant molecules to readily diffuse to the Ni²⁺ complex reaction sites in the vicinity of the metal NPs through inter-fiber voids. Plasmonic NPs (Ag or Au) and Ni²⁺ were immobilized on the alumina fibers in the procedure schematically illustrated in Figure 1. The transmission electron microscopy (TEM) images indicate that the metal NPs were dispersed throughout the γ -Al₂O₃ fiber support (Figures 2A and 2D). The supported Au NPs were relatively small, most of them smaller than 5 nm (Figure 2B and inset of Figure 2A), the mean particle size is 2 nm. The particle size distributions of the Ag NPs (Figure 2E and inset of Figure 2D) were broader, most of the Ag NPs were smaller than 15 nm and the mean particle size is about 9 nm. Line scan analysis (energy dispersion X-ray spectroscopy [EDX]) of plasmonic metal and Ni compositional fluctuations in Figures 2C and 2F indicate that the Ni²⁺ ions were immobilized on the bare support between the metal NPs, instead of accumulating on the surface of the plasmonic metal NPs.

The other structural and chemical properties of the catalyst were characterized by nitrogen adsorption, Fourier transform infrared spectroscopy (FTIR), X-ray diffraction (XRD), and X-ray photoelectron spectroscopy (XPS) and are shown in Table S2 and Figures S2–S6. The results verify that the photocatalysts possess the assembled structure as we designed.

Diffuse reflectance ultraviolet-visible (DR UV-vis) spectra of the samples are shown in Figures 2G and 2H. γ -Al₂O₃ fibers and grafted γ -Al₂O₃ fibers (ASN) have no obvious absorption in the visible-light region (wavelength > 400 nm), while two broad bands peaked at wavelengths of 378 and 652 nm are clearly observed for Al₂O₃-silane-NH₂-Ni²⁺ (ASN-Ni²⁺). These two bands can be assigned to the ³A_{2g}(F) → ³T_{1g}(P) and ³A_{2g}(F) → ³T_{1g}(F) transitions for distorted octahedral Ni²⁺ complexes.^{41,42} These absorption bands in 2.5Au-ASN-Ni²⁺ and 4.3Ag-ASN-Ni²⁺ samples overlap with the strong absorption of the supported metal NPs in the samples. Both 4.3Ag-ASN-Ni²⁺ and 4.3Ag-ASN samples have absorption bands centered at 405 nm, which are the LSPR absorption of Ag NPs.⁸ The 2.5Au-ASN-Ni²⁺ catalyst shows a broad light absorption and the absorption intensity decreases when the wavelengths are longer than 550 nm. No sharp characteristic LSPR peak of Au NPs at ~530 nm⁴³ is observed. This could be attributed to that the small Au NPs (with a mean size of 2 nm). The interaction of Au NPs with the amino group of the grafted silane also changes the electron density of the small Au NPs and their light absorption due to LSPR effect^{44,45} more significantly than that of the relatively larger Ag NPs (with mean size of 9 nm).

Photocatalytic Performance for Cleavage of Aryl Ether C–O Bonds

Figure 3 shows the catalytic performance for the C–O bond cleavage of benzyl phenyl ether (one of the α -O-4 model compounds) by the photocatalysts prepared

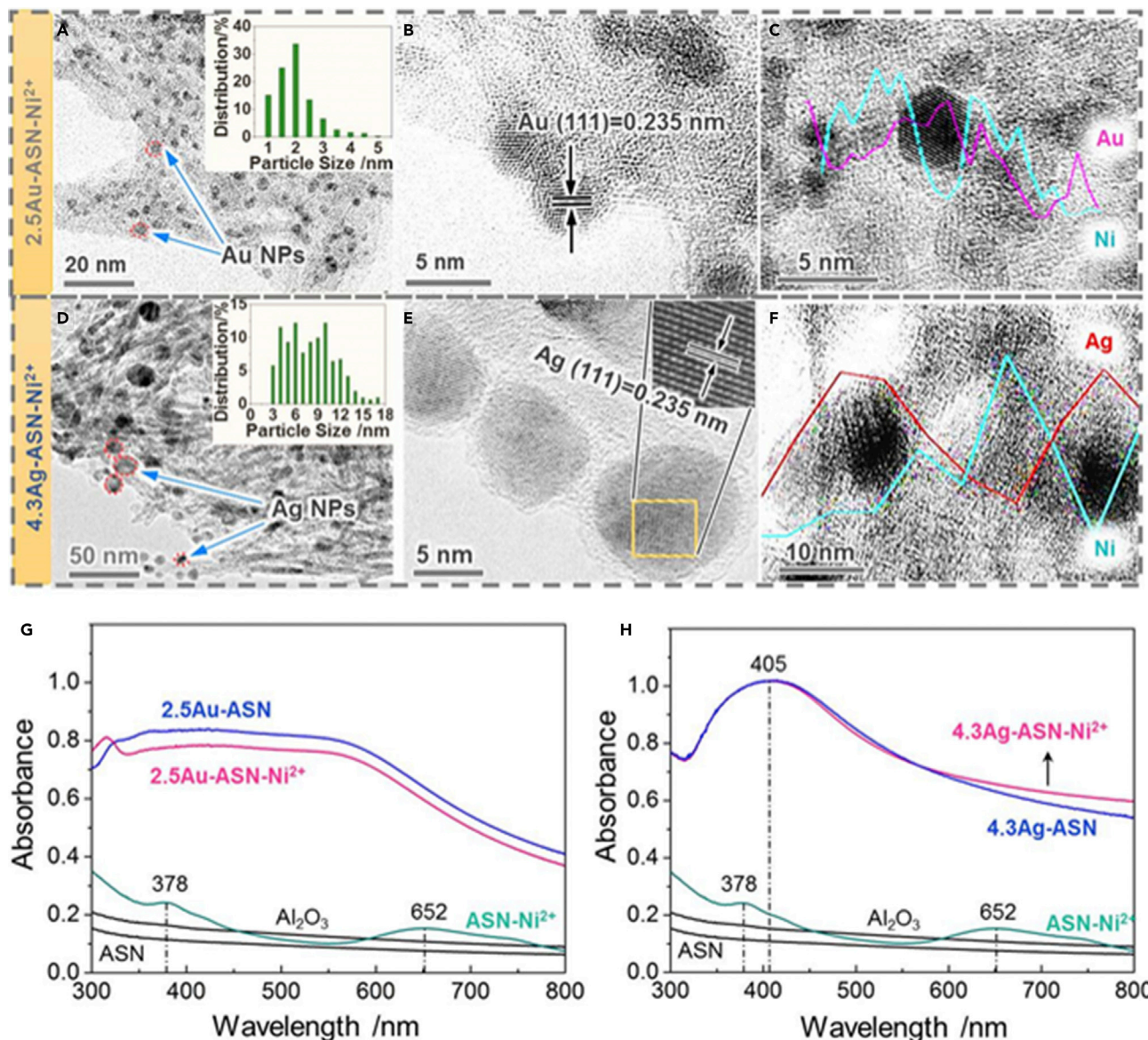


Figure 2. Characterization of the Photocatalysts

(A and D) TEM images of 2.5Au-ASN-Ni²⁺ (A) and 4.3Ag-ASN-Ni²⁺ photocatalysts (D); the insets are the particle-size distribution of the Au NPs and Ag NPs, obtained from measurement over 300 isolate particles in the TEM images.

(B and E) High-resolution TEM images of Au and Ag NPs on 2.5Au-ASN-Ni²⁺ (B) and 4.3Ag-ASN-Ni²⁺ (E).

(C and F) EDX line profile analysis of 2.5Au-ASN-Ni²⁺ (C) and 4.3Ag-ASN-Ni²⁺ (F).

(G and H) the UV-vis spectra of 2.5Au-ASN-Ni²⁺ (G) and 4.3Ag-ASN-Ni²⁺ (H).

with different amounts of plasmonic metal NPs (parameters given in the caption). Both the 2.5Au-ASN-Ni²⁺ and 4.3Ag-ASN-Ni²⁺ catalysts gave high conversion of the ether (98% and 96%, respectively) under visible-light irradiation of 0.96 W cm⁻², while no reaction was observed in the dark. The selectivity toward production of phenol was around 50%, indicating that a homolytic C–O bond scission of benzyl phenyl ether occurred. There are no products of undesired hydrogenolysis of aromatic rings; the high selectivity is because the moderate conditions of the photocatalytic process induce over-reduction.

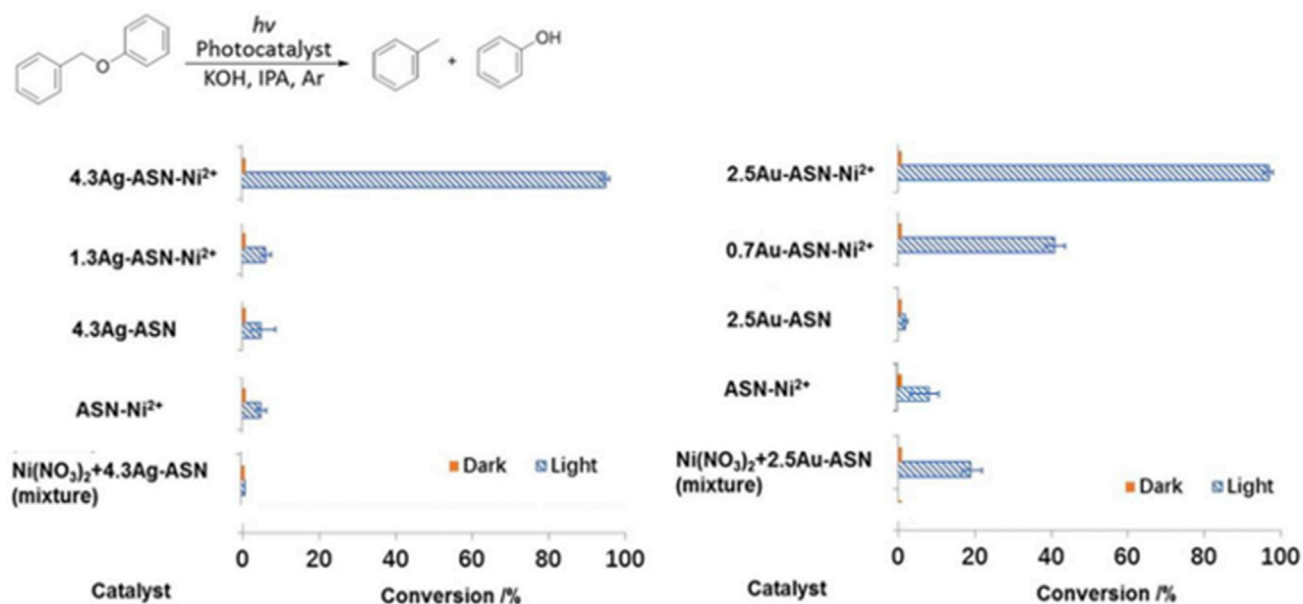


Figure 3. Catalytic Performances of the Assembled Photocatalysts for C–O Bond Cleavage of Benzyl Phenyl Ether under Visible-Light Irradiation and in the Dark

Reaction conditions: benzyl phenyl ether (0.05 mmol), KOH (0.15 mmol), and 2 mL of isopropanol (IPA) as solvent, mixed with 20 mg of catalysts in argon atmosphere. Light source was a halogen lamp with intensity of 0.96 W cm^{-2} , and the reaction was conducted at $80^\circ\text{C} \pm 2^\circ\text{C}$ for the systems with Ag NPs and $90^\circ\text{C} \pm 2^\circ\text{C}$ for the systems with Au NPs (the reactions with ASN-Ni²⁺ catalyst were conducted at $80^\circ\text{C} \pm 2^\circ\text{C}$ and $120^\circ\text{C} \pm 2^\circ\text{C}$ in the left and right panels, respectively) for 24 h. At these temperatures, a high reaction rate was achieved, while hydrogenation of the aromatic rings did not take place. Liquid specimens were sampled from the reaction mixture and measured by gas chromatography (GC). Error bars associated with conversion are the standard error of three sets of unique measurements.

The catalytic activities of a sample prepared with Ni²⁺ complexes but without the metal NPs, a sample with the metal NPs but no Ni²⁺ ions yielded very low conversion (6% or nil). This highlights a significant synergistic effect occurred when the Ni²⁺ complexes were immobilized in the presence of plasmonic metal NPs: when the light absorption by the metal NPs combines with the inherent catalytic capability of Ni²⁺ complexes, this results in superior photocatalytic activity of the composite. It is also evident that conversion of the reactant increased with increased metal NP loading of the catalyst. The synergistic effect becomes significant when the metal NP content is high.

Simply the mixture of Ni(NO₃)₂ and 4.3Ag-ASN exhibited negligible activity. Hence, the possibility that Ni²⁺ species in liquid phase are active for the catalytic reaction is excluded. The mixture of Ni(NO₃)₂ and 2.5Au-ASN exhibited a low conversion of about 20%. It appears that the gold NPs can interact with Ni²⁺ species in liquid while Ag NPs do not. The detailed reason is unknown. In those control experiments, the overall contents of Ni²⁺ ions and silver in the mixture of Ni(NO₃)₂ and 4.3Ag-ASN are the same as those in the 4.3Au-ASN-Ni²⁺. This is also the case for the Au sample. The significant differences in catalytic performance between the mixtures and our designed catalysts suggest that the interaction between metal NP-ASN and immobilize Ni²⁺ ions has substantial impact on the overall photocatalytic process, the reaction is a complete heterogeneous catalysis process for Ag-ASN-Ni²⁺ catalysts and proceeds mainly by heterogeneous catalysis process for Au-ASN-Ni²⁺ catalysts. Plasmonic NPs considerably enhance the catalytic activity of Ni²⁺ complexes only when they are immobilized in the close proximity to the NPs.

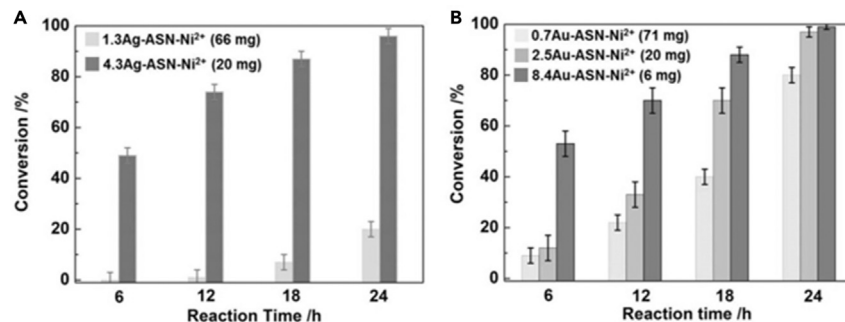


Figure 4. Impact of the Plasmonic Hot Spots on the Photocatalysis

The time course for the photocatalytic activities of xAg-ASN-Ni²⁺ (A) and xAu-ASN-Ni²⁺ (B) in C–O bond cleavage of benzyl phenyl ether (1.11 W cm⁻² of halogen light intensity at 80°C for Ag-Ni²⁺ system; 0.96 W cm⁻² of halogen light intensity at 90°C for Au-Ni²⁺ system). Error bars associated with conversion are the standard error of three sets of unique measurements.

Impact of the Plasmonic Hot Spots

It was reported that photothermal effect of plasmonic NPs could elevate the temperature of the NPs, which may play a critical role in the catalysis.⁴⁶ To understand if local heating will contribute to the Ni²⁺ catalysis, we conducted the photo-reaction using the ASN-Ni²⁺ catalyst at elevated temperatures (80°C–120°C); only 2% of conversion increase of C–O bond cleavage was observed (see Table S3), which means that a 40°C increase in reaction temperature could not enhance the catalytic activity of the Ni²⁺ complexes in our reaction system. Therefore, photothermal effect caused by irradiation could not drive the reaction in the present study. The hot electrons from the illuminated metal NPs may play the critical role in activating the aryl ether C–O bonds as is the case for some other plasmonic catalysts reported in the literature.^{1–13} But the Au and Ag NPs are not the active catalytic sites in the present study, as evidenced by the experimental data (see Figure 3). Hence, these catalysts may be expected to operate differently from the well-known mechanism where light-generated hot electrons promote reactions.^{2–8}

We compared the catalytic performance enhancement of Ni²⁺ when the number density of metal NPs are different by using catalysts with different metal NP contents and maintaining the metal NP content in the reaction systems and other experimental conditions identical. For instance, the reaction vessel was loaded with 66 mg of 1.3Ag-ASN-Ni²⁺ and 20 mg of 4.3Ag-ASN-Ni²⁺. The quantities of the two catalysts were calculated from the Ag content (Table S1). Figure 4A shows that the percent conversion of reactant in the reaction driven by 4.3Ag-ASN-Ni²⁺ is significantly higher than by 1.3Ag-ASN-Ni²⁺ although the content of immobilized Ni²⁺ ions in the latter is 3.8 times of that in the former (derived from data in Table S1). The turnover number (TON) with respect to the Ni²⁺ sites in 4.3Ag-ASN-Ni²⁺ was calculated from the conversion, being >18 times higher than that in 1.3Ag-ASN-Ni²⁺. Given that the Ag NP content in the two systems is the same, the overall Ag NP content in the catalytic system cannot be the reason for the large difference in the catalytic performance.

The major difference between the two photocatalytic systems shown in Figure 4A is that the Ag NPs are more closely packed in 4.3Ag-ASN-Ni²⁺. The junctions between closely spaced NPs can generate “hot spots” where the strong EM field coupling of the closely spaced NPs generates huge EM field enhancement.^{4,6} In a unit volume of catalyst, the Ag NPs in the 4.3Ag-ASN-Ni²⁺ is more than three times the Ag NPs in the 1.3Ag-ASN-Ni²⁺ catalyst, and therefore, there are a greater number of

nano-junctions between Ag NPs. The results in Figure 4A can be interpreted as a manifestation of the fact that the photocatalytic activity heavily depends on the number of Ag NPs' nano-junctions in the photocatalysts. An environment of high number density of Ag NPs can significantly promote catalytic performance of the immobilized Ni²⁺ complexes around the particles.

The effect of catalyst mass on photocatalytic activity was examined, and the results are provided in Table S4. The conversion increased as more catalysts were used. But the conversion did not increase linearly with catalyst mass. The deviation from the linearity may be attributed to the screen effect.

Figure S7 shows EDS mapping results of the 4.3Ag-ASN-Ni²⁺ photocatalyst, which reveals the existence of closely spaced NPs, consequently supporting the role played by plasmonic hot spots.^{21,22} Analysis of the results (Figure S7) indicates the distribution of plasmonic hot spots regions overlapped with concentrations of surface-bound Ni²⁺ complexes co-located in the plasmonic hot-spot regions.

A similar phenomenon can be found in the xAu-ASN-Ni²⁺ photocatalytic systems as seen in Figure 4B. However, the effect of high number density of Au NPs on the catalytic performance is weaker than that of Ag NPs. The performance improvement caused by increasing the number density of small Au NPs (from 0.7 wt % Au to 8.4 wt % Au; see TEM images in Figure S8) is less than that caused by increasing the number density of Ag NPs (from 1.3 wt % Ag to 4.3 wt % Ag; see TEM images in Figure S9).

We performed simulations of the near-field enhancement of single Au NP (2 nm) and dimer Au NPs (2 nm) with 1 nm gap between them (Figure S10) by using an electrostatic eigenvalue method; the details of the simulation methodology are from Davis and Gómez.⁴⁷ Under 400 nm excitation, the intensity of EM fields at the surface of an isolated Au NP is ~10 times larger than the field intensity of the incoming photon flux, while the enhancement of EM field occurring in the middle of the dimer is ~12 times. In contrast, the EM field localization upon LSPR excitation of Ag NPs is significantly higher (Figure S11). The intensity of EM fields at the surface of an Ag NP (9 nm) is ~300 times larger than the field intensity of the incoming light, while the enhancement of EM field occurring at the hot spot of the dimer is ~8,000 times. The hot spot regions will have high concentrations of energetic electrons (because the high number density of the plasmonic NPs) and interaction of the EM near-field with reactant in these regions is likely to be very strong. Thus, these sites are considered most important for plasmonic photocatalysis.

We note that our wet-chemistry synthesis approach results in distributions of sizes of the plasmonic metal particles and a range of inter-particle distances in the catalysts as previously reported.^{1,2} Uniform metal particle size and inter-particle distance is not a prerequisite for formation of plasmonic hot spots.⁴⁶ The 4.3Ag-ASN-Ni²⁺ catalyst has many more hot spots, compared to 1.3Ag-ASN-Ni²⁺ as shown in Figure S9. The intense field enhancement at the hot spots between the metal NPs clearly influences the catalytic performance of Ni²⁺ complexes under mild reaction conditions, and the results of Figure 3 represent a statistical average which is dominated by the response augmented by plasmonic hot spots.

The existence of hot spots has also been experimentally observed. Highly intense EM near-fields affect the properties of molecules within them;⁴⁸ for example, the intensity of signals in surface-enhanced Raman scattering (SERS) of the molecules.^{48–50}

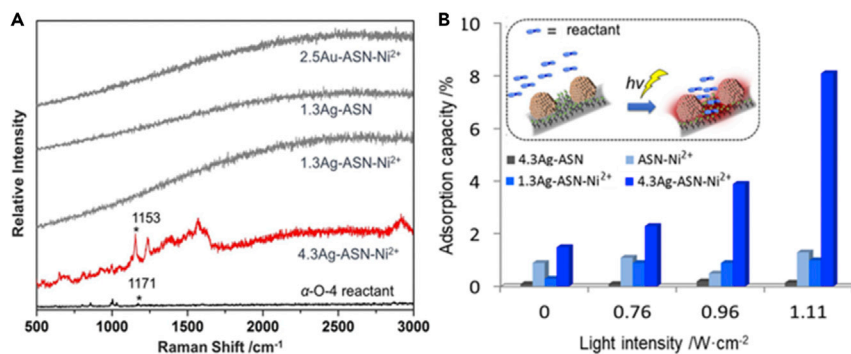


Figure 5. Light-Enhanced Adsorption

(A) Surface-enhanced Raman spectra of benzyl phenyl ether adsorbed on 2.5Au-ASN-Ni²⁺, 1.3Ag-ASN(-Ni²⁺), and 4.3Ag-ASN-Ni²⁺ photocatalysts. The characteristic vibration of the C–O bond from the reactant is marked with an asterisk. The samples were prepared by mixing 10 mg of catalysts with 0.5 mL of the ether in IPA (0.5×10^{-2} M) for 6 h at room temperature and dried at 60°C in a vacuum oven overnight. The instrument is equipped with a laser with 532 nm of wavelength.

(B) The comparison of adsorption properties of catalysts for benzyl phenyl ether. In a typical procedure, 20 mg of catalyst was added to 2 mL of adsorbate/IPA (0.5×10^{-2} M) solution, filled with argon, and sealed. The adsorption was conducted for 10 h at 80°C, the same temperatures designated for the reaction. Only the ether and IPA can be detected by GC, for KOH is absent in the experiment. Inset schematically shows optical plasmonic trapping of the reactant.

SERS predominantly originates from EM near-field enhancement, and its intensity is approximately proportional to the square of the EM field intensity. Thus, the intensity of SERS active peaks of reactant is expected to be commensurate with intensity of the enhanced EM near-field around Ag NPs experienced by the reactant molecules. The Raman spectra of benzyl phenyl ether adsorbed on the catalysts with different Ag NP contents were compared (seen in Figure 5A).

The results show that when the aryl ether molecules were adsorbed on the catalysts with a high content of Ag NPs (4.3Ag-ASN-Ni²⁺), peaks at $1,153 \text{ cm}^{-1}$ ascribed to the aryl ether C–O bond vibration become much more intense, even when compared to their concentrated counterpart (pure benzyl phenyl ether). No SERS signals were detected with the catalyst samples prepared with a lower Ag NP content (1.3Ag-ASN-Ni²⁺ and 1.3Ag-ASN) or with small Au NPs. Given that the photocatalysts have a similar specific surface area (Table S2), the adsorption of the aryl ether molecules on the alumina support has no obvious effect on the Raman signal intensity. The SERS results can be attributed to three possibilities: (1) there is a higher concentration of the aryl ether adsorbed on the samples with a higher Ag NP content; (2) the EM near-field is much more intense (there are more hot spots) in the photocatalysts with increased number density of Ag NPs, and this significantly enhances the Raman signal of adsorbed molecules; or (3) the pronounced Raman signals are due to synergistic effect of the two reasons above. The near-field enhancement of the sample with small Au NPs (the 2.5Au-ASN-Ni²⁺) is relatively weak as indicated by the simulation results and the fact that there is no LSPR absorption peak at about 520 nm wavelength. This is consistent with the result that no enhanced Raman signal is observed.

Light-Enhanced Chemisorption

The reactant adsorption is a key step prior to surface reaction in heterogeneous catalysis, the impact of light irradiation on the adsorption has not been extensively investigated to date. To explore whether the light irradiation can affect reactant adsorption, we conducted adsorption experiments of benzyl phenyl ether on

different catalysts in the dark and under light irradiation with different light intensities. The results are summarized in Figure 5B. The adsorption amount is given by the percentage of the initial concentration of the reactant before light irradiation, which was adsorbed by the catalyst under irradiation. The adsorption capacity is calculated based on the Ni amount collected in Table S1. In the experiment, the cleavage reaction did not proceed as KOH was not added. No chemicals other than those added were detected. The adsorption capacity (AC) was calculated as

$$AC(\%) = 0.01 \times \left(\frac{C_0 - C}{C_0 n_{Ni}} \right) \times 100,$$

where 0.01 is the total molar amount of benzyl phenyl ether, C_0 and C are the concentrations of the ether before and after adsorption experiment, respectively, and n_{Ni} is moles of nickel (calculated by the data shown in Table S1). The adsorption properties of ASN-Ni²⁺, 1.3Ag-ASN-Ni²⁺, and 4.3Ag-ASN-Ni²⁺ catalysts are compared in Figure 5B.

The initial concentration used for the adsorption experiment (0.01 M) was much lower than that used in the reaction. The amount of Ni²⁺ (the adsorption site) in these samples was 0.011–0.013 mmol, and as discussed below, only the adsorption on a fraction of the Ni²⁺ sites, which are in the intense EM fields, was influenced by light irradiation. When a high initial concentration of reactant was added, it was difficult to accurately detect the concentration changes caused by light-induced adsorption.

It is also worth noting that only trace amounts of benzyl phenyl ether were adsorbed on the illuminated 4.3Ag-ASN catalyst, the sample without Ni²⁺ but with high Ag NP content. This implies that the EM near-fields alone are not leading to increased reactant adsorption. One needs to consider the interaction between the ether and Ni²⁺ complex sites of the catalysts too. We measured FTIR spectra of the catalysts after the ether adsorption experiments (Figure S12). For the ASN-Ni²⁺ samples that adsorbed the ether in the dark or under light irradiation of intensity of 1.11 W cm⁻², the position of the peak located at 1,151 cm⁻¹ (which is assigned to the C–O bond stretch mode of the ether) remains unchanged (Figures S12A and S12D).

However, for both catalysts containing Ag NPs and the surface-bound Ni²⁺ complexes (1.3Ag-ASN-Ni²⁺ and 4.3Ag-ASN-Ni²⁺), this band is blue-shifted to a higher wavenumber under light-irradiation conditions. This indicates an enhanced interaction can occur between the ether and Ni²⁺ sites when hot spots are activated (Figures S12E and S12F). Also, the intensity of the band at 1,350 cm⁻¹ (the vibration mode of NO₃⁻ that coordinates with Ni²⁺ sites) decreased markedly after the sample was illuminated (Figures S12B and S12C). This can be explained if NO₃⁻ is displaced by the ether during adsorption under visible-light irradiation. The light-induced adsorption of the ether is irreversible since it remained adsorbed after the light was switched off. The specific adsorption sites (Ni²⁺ sites), the coordination of the adsorbate to the sites, the requirement of activation energy (light harvested by the plasmonic metal NPs) for the adsorption, and irreversible adsorption process suggested chemisorption of the ether at Ni²⁺ sites.

The adsorption of the ether increases significantly with the light intensity increases, on the photocatalyst 4.3Ag-ASN-Ni²⁺ (Figure 5B). The adsorption of the ether on 1.3Ag-ASN-Ni²⁺ catalyst (with much less hot spots) is considerably lower, regardless of the light intensities used. These data demonstrated that the ether adsorption depends on the number density of Ag NPs and intensity of the incident light but not on the overall number of Ni²⁺ complexes in a sample. The higher light intensity and the

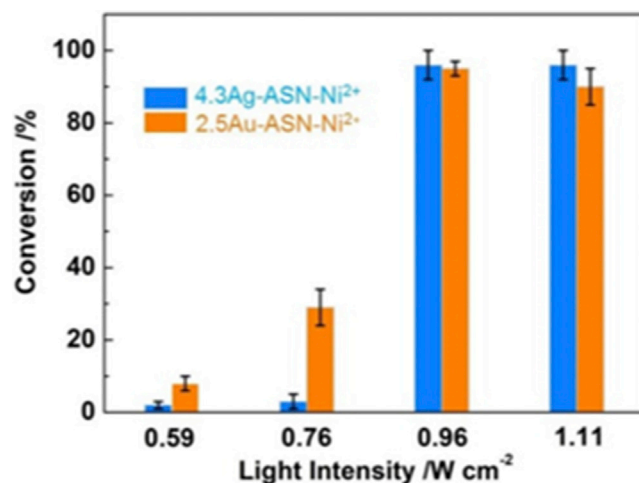


Figure 6. The Dependence of Photocatalytic Activities of 2.5Au-ASN-Ni²⁺ and 4.3Ag-ASN-Ni²⁺ Photocatalysts for Benzyl Phenyl Ether Cleavage on the Intensity of the Light Irradiation

The reactions were conducted at 80°C and 90°C for Ag NP and Au NP systems, respectively. Error bars associated with conversion are the standard error of three sets of unique measurements.

Ag NPs density determine the stronger EM near-fields generated close to the active sites Ni²⁺. 1.3Ag-ASN-Ni²⁺ sample contains slightly more Ni²⁺ complexes than the 4.3Ag-ASN-Ni²⁺ sample (Table S1). It follows that the chemisorption only appears at the Ni²⁺ sites subject to the EM fields of high intensity. In 1.3Ag-ASN-Ni²⁺, a small number of sites with the sufficient EM field intensity for chemisorption as the sample has small number of hot spots. Increasing the incident light intensity amplifies the intensity of the EM near-fields, and as the number of such sites increases, so does the chemisorption. Such an increase is insignificant for 1.3Ag-ASN-Ni²⁺ compared with that for 4.3Ag-ASN-Ni²⁺. To the best of our knowledge, there have been no reports on light-enhanced chemisorption of molecules with irradiation of continuous-wave visible-light of moderate intensity ($\sim 1 \text{ W cm}^{-2}$). Very recently, we reported that a plasmonic alloy system can selectively concentrate the reactant molecules to catalyst surface and thus increase the reaction rate by several orders under light.⁵¹ It is proven that light irradiation generates an optical plasmon force that can add to van der Waals force and selectively attract reactant molecules to the active sites. In the plasmonic antenna system in the present study, similar optical plasmon force contributes to concentrate the ether to catalyst surface and thus enhances the chemisorption of ether on Ni²⁺ sites. This provides essential knowledge on how visible-light irradiation significantly promotes the catalytic performance of metal cations by plasmonic metal.

Light-Intensity Dependence of Catalytic Performance

Following the chemisorption, the dependence of photocatalytic performance on the intensity of the light source is also investigated in Figure 6. The temperature of the reaction mixture was carefully maintained at 90°C or 80°C \pm 2°C to guarantee that thermal effects could be discounted. It is clear that the higher the light intensity, the greater is the contribution of light irradiation to driving the reaction. When the light intensity is 0.96 W cm⁻², over 90% of the conversion is due to light irradiation for the C–O bond cleavage of benzyl phenyl ether. Clearly, light irradiation is the principle driving force of the reaction. Higher light intensity generates more hot electrons in metal NPs and also generate stronger EM field to increase the reactant chemisorption; thus, irradiation-induced enhancement of chemisorption and reactant conversion are correlated.

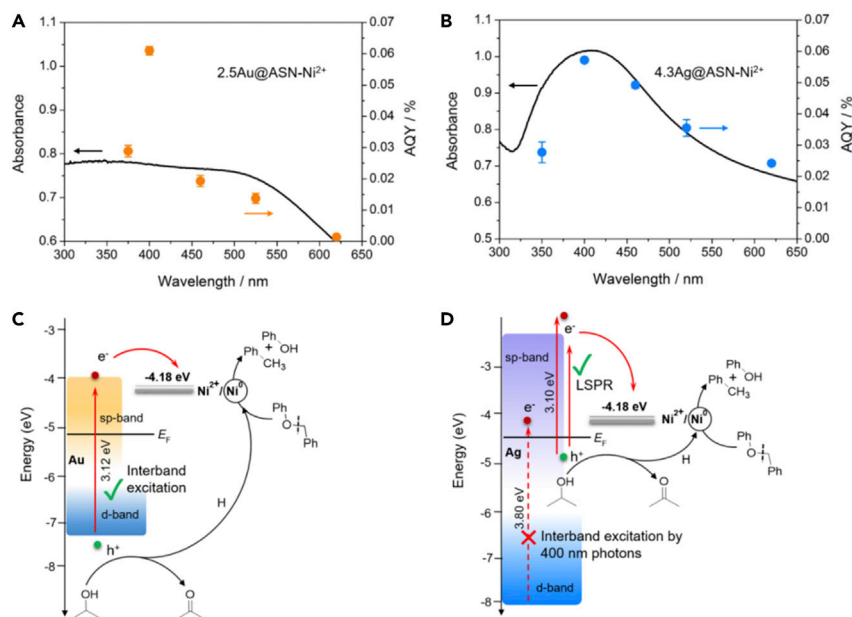


Figure 7. Effects of Light Wavelength for Benzyl Phenyl Ether Cleavage and the Energy Alignment

(A and B) The dependence of photocatalytic activities of 2.5Au-ASN-Ni²⁺ (A) and 4.3Ag-ASN-Ni²⁺ (B) on the light-irradiation wavelength. Error bars associated with conversion and AQY (y axis on the right-hand side) are the standard error of three sets of unique measurements. The light intensity for all wavelengths is the same (0.2 W cm⁻²). The UV-vis spectrum of the photocatalyst is also provided for comparison.

(C) Energy diagram of *d* band and Fermi level of Au and Ni²⁺/Ni⁰ reduction potential.

(D) Energy diagram of *d* band and Fermi level of Ag and Ni²⁺/Ni⁰ reduction potential.

Correlating the light intensity dependence of the chemisorption and the reactant conversion with observation that the catalytic performance is not regulated by the overall Ni²⁺ content in the photocatalyst system (Figure 4A), we infer that the C–O bond cleavage predominantly takes place on the Ni²⁺ sites within the hot spots, where the ether molecules chemically adsorbed. The adsorbed ether molecules will experience an intense oscillating EM field, which could facilitate the activation of the molecules for the cleavage reaction. The hot spots can capture both light energy and reactant molecules, have higher concentration of hot electrons and thus, are an ideal location for the catalysis.

Besides, as can be seen in Figure 6, increasing the light intensity to higher than 0.76 W cm⁻² resulted in a dramatic increase in the conversion of the C–O bond cleavage reaction catalyzed by 2.5Au-ASN-Ni²⁺ (or 4.3Ag-ASN-Ni²⁺). There exists an energy threshold to activation of benzyl phenyl ether molecule. It is between 0.59 and 0.76 W cm⁻² for 2.5Au-ASN-Ni²⁺ catalyst at 90°C and between 0.76 and 0.96 W cm⁻² for 4.3Ag-ASN-Ni²⁺ at 80°C. The intensity threshold is a common feature in photocatalysis systems mediated by plasmonic NPs and influenced by various factors.⁵²

Influence of Light-Irradiation Wavelength (Energy Alignment)

The catalytic performance variation with the wavelength reveals the energy alignment of the combined system. The action spectrum (Figures 7A and 7B) shows the dependence of the irradiation wavelength on the conversion efficiency of the

photocatalytic reactions. The reaction rates were converted to the apparent quantum yields (AQYs), which were calculated as

$$\text{AQY (\%)} = \frac{Y_{\text{light}} - Y_{\text{dark}}}{n} \times 100,$$

where the Y_{light} and Y_{dark} are the amount of reactant being converted under light irradiation and dark conditions, respectively;¹⁵ n is the number of incident photons. The number of reactant being cleaved in the dark, Y_{dark} , was subtracted from that observed when the system was irradiated, Y_{light} , to clearly illustrate the contribution of light irradiation to the overall conversion. The AQY is a wavelength-dependent quantity that is given by the ratio of the number of molecules produced to the number of incident photons. By definition, it is a quantity that is independent of the intensity of the incident radiation, and its trend provides physical insight on the mechanism, accounting for the conversion of photonic energy into chemical potential energy.

For the Ag-Ni²⁺ photocatalytic system, the highest conversion rate was achieved when illuminating with a 400 nm peak wavelength (Figure 7B). According to the UV-vis spectra of the photocatalyst in Figure 2H, the most intense LSPR absorption of Ag NPs in this photocatalyst occurs at 405 nm, well matched with the LED wavelength with which the highest cleavage reaction rate conversion was observed. Also, the AQY spectrum generally matches the absorption of photocatalyst (Figure 7B). Given the temperature of the reaction mixture and the irradiation energy of each wavelength were carefully maintained identical, the significant AQY variation with irradiation wavelength corroborates that the reaction was mainly driven by light. The results evidence that the enhancement of the catalytic performance is caused by the LSPR absorption of Ag NPs. The LSPR absorption in the range between 400 and 600 nm can generate hot electrons with sufficient energy to reduce Ni²⁺ in the complexes.

For the 2.5Au-ASN-Ni²⁺ photocatalyst, the AQYs show a mismatch with the catalyst light absorption: the highest conversion rate was achieved when illuminating with a 400 nm peak wavelength (single-color LED source with band width ± 10 nm), while there is no absorption peak at this wavelength (Figure 7A). Hence, light absorption is not the sole factor determining the catalytic reaction over the small Au NPs. The high AQY at 400 nm suggests that there is an energy alignment governing the electron transfer: only hot electrons of sufficient energy can trigger the reaction that takes place at Ni²⁺ complex sites.

According to the diagram shown in Figure 7C, photons with 397 nm wavelength (~ 3.12 eV) are able to excite d electrons of Au NPs to the energy level for Ni²⁺ reduction. Photons with longer wavelengths have insufficient energy to reduce Ni²⁺ ions. On the other hand, a much lower reaction rate is observed under irradiation with wavelength < 380 nm (Figure 7A). It has been reported that visible-light illumination can make the reduction potential of Ni²⁺ complex shift negatively.⁵³ We also found that the UV irradiation shifted Ni²⁺/Ni⁰ reduction potential by 0.2 eV increasing the difficulty in reduction of Ni²⁺ complexes. Another possible reason is that light with wavelength around 380 nm causes the ${}^3A_{2g}(F) \rightarrow {}^3T_{1g}(P)$ transition for the distorted octahedral Ni²⁺ complex (which exhibits light absorption peaked at 378 nm). A fraction of light can be absorbed for this transition; accordingly, fewer hot electrons are generated. Consequently, the reduction of Ni²⁺ complex, which is critical for the C–O bond cleavage as discussed later, proceeds at a slow rate. Therefore, there is a narrow energy window at about 3.12 eV, in which photons generate hot electrons

by interband electron excitation in the Au NPs to reduce Ni^{2+} ions driving the reaction. The energy alignment in Figures 7C and 7D may not be strict as the alignment is affected by other factors such as temperature, pH, and solvent. However, it provides a good approximation of the alignment. As shown in Figures 7C and 7D, isopropanol acts as a sacrificial electron donor and is oxidized into acetone on the metal particles,^{2,15} accomplishing the electron-hole separation in high efficiency.

In contrast, the energy level of *d* band in silver is much lower than that in gold⁵⁴ so that the hot electrons generated by interband transition in Ag NPs do not have sufficient energy to reduce Ni^{2+} ions directly (Figure 7D).

Interband Electron Excitation of Small Au NPs

The catalysts with Au NPs or Ag NPs have similar architecture but distinct differences in LSPR absorption characteristics. The weak LSPR absorption of the small Au NPs (seen in Figure 2G) can be expected to generate a much weaker EM near-field. The EM field enhancement at the hot spots of small Au NP dimer is also predicted to be weak (Figure S10). Hence, the LSPR absorption is possibly too weak to be the main driving force for promoting the reaction. Light-excited interband transition (from *d* band to *sp* band) in the small Au NPs should be main mechanism for generating hot electrons that induce the catalytic reaction.

Interestingly, light-induced adsorption phenomenon occurred in 2.5Au-ASN- Ni^{2+} photocatalytic system as well (Figure S13). It is known that metal NPs produce large field gradients in a wide wavelength range (not only LSPR wavelength)⁵⁵ as the oscillating EM field of incident light always changes the charge distribution of metal NPs. Also, electrical charges tend to accumulate in sharp edges and high curvature surface of metal particles (lightening rod effect). The higher charge density at surface of the smaller particles results in sharper gradient around the particles. The two effects are applicable to small Au NPs, leading to the increasing chemisorption under light irradiation.

Molecular Bridge for the Hot Electron Transfer and Ni^{2+} Reduction

The above observation implies that the reaction is operated via the transfer of energy and light-excited hot electrons from metal NPs to Ni^{2+} active sites, modulating the oxidation state of Ni^{2+} in the process. In many reactions catalyzed by the transition-metal complexes, the change in the oxidation state of the transition metal enables the bond-breaking or bond-forming processes (oxidative addition and reductive elimination).²³

The electron paramagnetic resonance (EPR) spectra of the photocatalysts shown in Figure 8 support our inference. The EPR spectra of the photocatalysts (4.3Ag-ASN- Ni^{2+} and 2.5Au-ASN- Ni^{2+}) with the reactant benzyl phenyl ether and solvent isopropanol (IPA) after purple light irradiation (400 nm of wavelength) exhibits a six-line signal (traces b and d in Figure 8), which is similar to that observed from the ASN- Ni^{2+} sample after reduction in H_2 atmosphere at 200°C (trace e in Figure 8). The *g*-factor (~ 2.01) is close to the reported Ni NPs with a characteristic of paramagnetic behavior.⁵⁶ So a fraction of the nickel in this H_2 reduced sample exists in the Ni^0 state. The paramagnetic signals are not observed in the spectra of other samples, even the system of the photocatalysts in IPA solvent after light irradiation (without the ether, see Figure S14). The results indicate that in the presence of the ether, a $\text{Ni}^{2+} \rightarrow \text{Ni}^0$ transformation takes place in the photocatalyst under irradiation of 400 nm. The hot electrons generated on the illuminated metal NPs migrate to the Ni^{2+} complex and reduce Ni^{2+} ion to Ni^0 . However, the results shown in trace d in

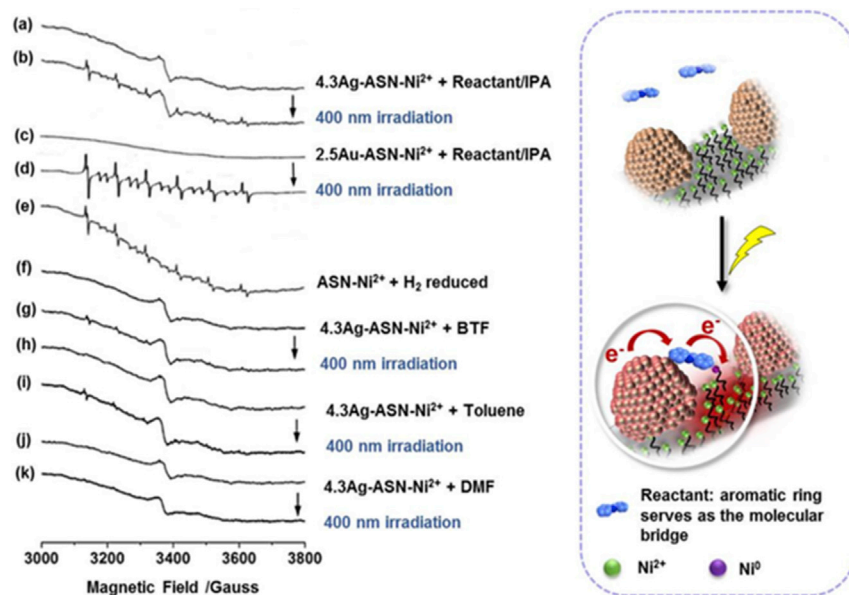


Figure 8. EPR Spectra of the Photocatalytic System before and after Irradiation under Light with 400 nm Wavelength

The concentration of α -O-4 reactant is 0.1 M; the EPR measurement was conducted at room temperature. Inset: schematically shown the reactant molecular serves as a “molecular bridge” for the transfer of the photo-induced hot electrons from the Ag(Au) NPs to Ni^{2+} sites.

Figure S14 that direct electron transfer from Ag NPs to the Ni^{2+} complex is not evidenced by the EPR spectrum of the photocatalyst dispersed in IPA solvent in the absence of α -O-4 reactant under irradiation of 400 nm wavelength. It seems that the ether molecules are involved in the reduction of Ni^{2+} to Ni^0 . Surprisingly, we observed the $\text{Ni}^{2+} \rightarrow \text{Ni}^0$ reduction after illumination, when the photocatalyst was dispersed in benzotrifluoride (BTF) or toluene (traces f-i in Figure 8) in the absence of the ether, but this phenomenon was not observed when BTF was replaced with N,N-dimethyl-formamide (DMF) (traces j and k in Figure 8). It has been reported that for the C-C stretching modes of unsaturated hydrocarbons, temporary electron transfer from plasmonic metal NPs into the normally unoccupied anti-bonding π^* orbitals can happen in a SERS system.⁵⁷ Therefore, the aromatic ring in the molecules of the aryl ether, BTF, and toluene could serve as a “molecular bridge” for the transfer of the photo-induced hot electrons from the plasmonic metal NPs to Ni^{2+} sites (inset in Figure 8). The hot electrons have sufficient energy to migrate to the unoccupied anti-bonding π^* orbitals of the aromatic ring.

For the Au- Ni^{2+} system, the ether molecules are also necessary for the charge transfer process to produce Ni^0 state species (comparing the results of trace d in Figure 8 and trace a in Figure S14). So generation of hot electrons on Au NPs surface is a prerequisite but not sufficient condition. The transfer of the hot electrons plays a critical role in the Ni^{2+} reduction.

No products were detected when toluene or BTF was used as the solvent (Table S5), suggesting that the IPA is necessary in the reaction as the hydrogen source for the reductive cleavage. The reducing agent IPA adsorbed on the surface of Ag NPs or Au NPs releases H atoms at the surface and is itself oxidized as a sacrificial electron donor in the presence of KOH and acetone was detected.² Using IPA as reduction agent avoids high pressure H_2 that has a safety risk. The aryl ether molecules adsorbed

at Ni^{2+} complex sites, and molecules with aromatic rings could assist transfer of the light-generated hot electrons from the illuminated NPs to Ni^{2+} sites. The reduced Ni^0 state is chemically unstable in the reaction environment because the reductive potential of $\text{Ni}^0/\text{Ni}^{\text{II}}$ (-1.2 V versus SCE)²⁸ is more negative than that of benzyl phenyl ether (-0.62 V versus SCE, seen in Figure S15). Therefore, the reduced Ni^0 sites could catalyze the cleavage of the C–O bonds in the aryl ether compound. Given the dependence of the chemisorption on the EM near-field intensity and the required molecular bridge for the hot electron transfer, the reaction should take place predominately at the Ni^{2+} complex sites which are simultaneously close to the metal NPs and subject to intense EM fields, i.e., within plasmonic hot spots.

The efficiency of electron transfer by benzyl phenyl ether bridge should be also correlated to the ratio of NP to Ni^{2+} . The mean density of the Ag NPs and Au NPs are estimated and summarized in the Table S6 and correlated to mean densities of APTMS and Ni complexes. The distributions of supported NPs and Ni^{2+} complexes based on the mean densities are presented as below. The densities are averaged data, summarized from TEM images in Figures 2, S8, and S9. The Ag NPs density in 4.3Ag-ASN- Ni^{2+} sample is 8 times of Ag NPs density in 1.3Ag-ASN- Ni^{2+} sample. The density of the Ag and Au NPs determines the ratio of NP: Ni^{2+} . The higher the NP: Ni^{2+} ratio, the higher the efficiency of electron transfer by benzyl phenyl ether bridge. Thus, the electron transfer efficiency in 4.3Ag-ASN- Ni^{2+} is much higher than in 1.3Ag-ASN- Ni^{2+} because there are 36 Ni^{2+} corresponds to per Ag NP in 4.3Ag-ASN- Ni^{2+} and 508 Ni^{2+} corresponds to per Ag NP in 1.3Ag-ASN- Ni^{2+} . Similarly, the Au NP: Ni^{2+} ratio in 8.4Au-ASN- Ni^{2+} is much higher (1:10) than the other two catalysts, 1:17 and 1:47. The electron transfer by benzyl phenyl ether bridge in 8.4Au-ASN- Ni^{2+} and 2.5Au-ASN- Ni^{2+} catalysts is more efficient than that in 0.7Au-ASN- Ni^{2+} catalyst.

The Mechanism of the Cleavage Reaction

On the basis of these results, we propose a tentative reaction pathway for the cleavage, the main features are depicted in Figure 9. The aryl ether molecules first diffuse within the framework of the photocatalyst and physically adsorb onto the catalyst surface (the adsorption observed in the dark; Figure 5B). Visible-light irradiation induces chemisorption of the ether at Ni^{2+} complex sites (i-ii), the ether molecules coordinate to Ni^{2+} ions replacing the NO_3^- ions. Then photo-generated hot electrons transfer to Ni^{2+} sites (via the unoccupied anti-bonding π^* orbitals of the aromatic ring of the ether) and reduce the ions to Ni^0 species (iii). The reduced Ni^0 species can catalyze the C–O bond cleavage, as described by literature reports,^{37,58} yielding the final products (v). Here, IPA is oxidized on the plasmonic metal NPs (iv), similar to the mechanism reported.² The IPA oxidation releases hydrogen and electrons, which are needed in hydrogenolysis. The synergistic effect between the optical antenna function of plasmonic metal NPs and the catalytic ability of Ni^{2+} sites dominates the transformation of the aryl ether. The synergistic effect is accredited to light-induced chemisorption of reactant molecules and the generation and function of the hot electrons as shown in Figure 9.

The stability and recyclability of the catalysts investigated. The silane was grafted onto the Al_2O_3 support in toluene at 110°C , so that the Al–O–Si bond is stable at the reaction temperatures (80°C and 90°C). We compared the contents of Si in 4.3Ag-ASN- Ni^{2+} and reused 4.3Ag-ASN- Ni^{2+} photocatalysts measured by the EDX (Figure S16), they are similar (2.2–2.4 wt %). The recycle stability of the photocatalyst is illustrated in Figure S16. The 4.3Ag-ASN- Ni^{2+} catalyst was reused for 3 cycles of C–O bond cleavage of benzyl phenyl ether under light irradiation. The

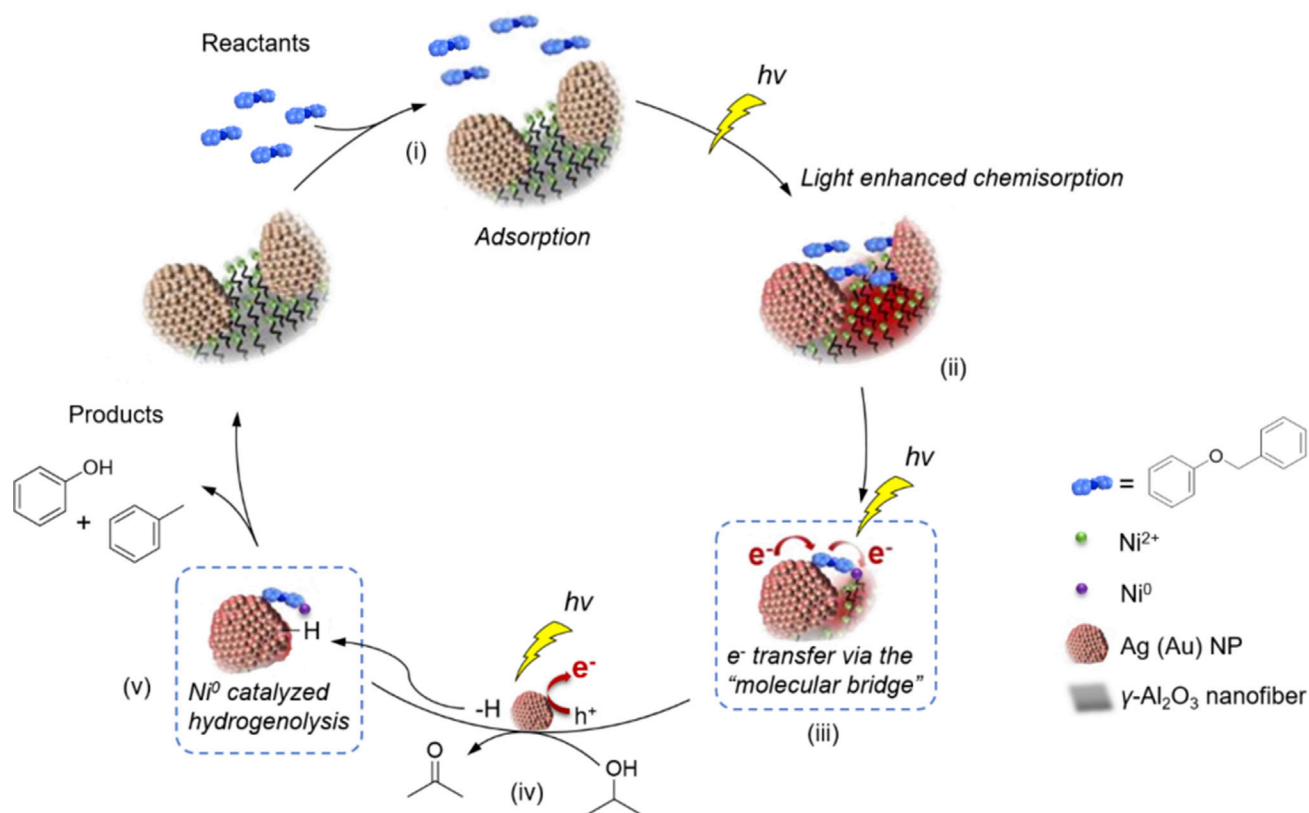


Figure 9. Proposed Mechanism for the Photocatalytic C–O Bond Cleavage of Benzyl Phenyl Ether with the Photocatalyst

product conversion moderately decreased during recycling, and the leaching of Ni^{2+} ions during the reaction caused the decrease in Ni content of the used catalyst. The soluble Ni^{2+} ions were not active for the hydrolysis at 80°C . The decrease could also be due to the partial loss of Ag NPs on the external surface of aggregates of randomly oriented fibers and leaching of nickel, thus lowering the chemisorption of reactant amount and formation possibility of Ni^0 species, as seen in the EDS mapping result displayed in the figure.

CONCLUSIONS

In summary, with the designed photocatalyst structure we have demonstrated that Au NPs or Ag NPs can act as optical antennas to absorb visible-light and promote the catalytic performance of Ni^{2+} complex immobilized in the hot spots. The new plasmonic-antenna-promoted catalysts with 2.5 wt % of small Au NPs (~ 2 nm) or 4.3 wt % of Ag NPs (~ 9 nm) exhibited superior catalytic activity for the cleavage of relative stable C–O bonds in benzyl phenyl ether under visible-light irradiation and mild reaction conditions without reduction of the aromatic rings. The results signify a new mode to activate chemical reactions by combining the advantages of plasmonic metal NPs and the chemical bond formation ability of transition-metal complexes, which is complementary to known plasmonic catalysis and transition-metal complex catalysis.

We have provided strong evidence suggesting that the catalytic performance is enhanced by the synergy of the following two effects: hot-electron transfer to the catalytically active Ni^{2+} complex sites and light-enhanced chemisorption of reactant

species. Both of these effects are greatly augmented by the strong EM near-field localization attainable with plasmonic hot spots. The energy alignment is commonly a key issue for the hot-electron transfer in the new photocatalysts. We believe these results will stimulate further research into the creation of novel plasmonic-antenna-promoted catalysts that exploit the high chemical reactivity of transition-metal complexes.

EXPERIMENTAL PROCEDURES

Materials

The chemicals were purchased from commercial suppliers and used as provided: benzyl phenyl ether (Sigma-Aldrich, >98%), isopropanol (Sigma-Aldrich, >99.5%, anhydrous), toluene (Fisher, >99.99%, GC assay), N,N-dimethyl formamide (Sigma-Aldrich, >99.8%, anhydrous), α,α,α -trifluorotoluene (Sigma-Aldrich, >99%, anhydrous), acetic acid (Ajax Finechem, >99.7%), nitric acid (Ajax Finechem, 68%–70%), C₁₂₋₁₄H₂₅₋₂₉O(CH₂CH₂O)₅H surfactant (Sigma-Aldrich), (3-aminopropyl)trimethoxysilane (Sigma-Aldrich, >97%), potassium hydroxide (Sigma-Aldrich, >99.99%), phenol (Ajax Finechem, AR), silver nitrate (Merck, AR), gold chloride trihydrate (Sigma-Aldrich, >99.9%), nickel(II) nitrate hexahydrate (Scharlau, >98%), sodium borohydride (Sigma-Aldrich, >98%), sodium aluminate (Sigma-Aldrich, anhydrous), H₂ (Supagas, >99.999%), and Ar (Supagas, >99.99%)

Catalyst Preparation

The photocatalysts were prepared following the illustration shown in Figure S1. γ -Al₂O₃ nanofibers were prepared following a procedure reported previously⁵⁹ and used as support of the catalysts. Boehmite (with a chemical formula of AlOOH) nanofibers were prepared from NaAlO₂ and then converted to γ -Al₂O₃ fibers by calcination at 450°C for 5 h. The details of the fiber preparation are provided in the Supplemental Information. Amino groups were then grafted on 3.0 g of γ -Al₂O₃ fibers by refluxing in 50 mL of toluene solution of 9.7 mmol of (3-aminopropyl)trimethoxysilane (APTMS) for 40 h. The solid sample was collected by washing and filtrating with H₂O and ethanol, and finally dried at 60°C (Al₂O₃-silane-NH₂ is abbreviated to ASN).

Plasmonic Ag or Au NPs were prepared on ASN support by an impregnation-reduction procedure. For example, in the synthesis of 1.3 wt % of Ag NPs on ASN support, 1.0 g of the ASN support was dispersed into 133 mL of deionized water under vigorous stirring with a magnetic stirrer for 20 min. 27.8 mL of 0.01 M AgNO₃ aqueous solution was then added to the suspension and stirred for further 20 min. Next, 74 mL of NaBH₄ (0.038 M) aqueous solution was added dropwise to the suspension over 30 min under continuous stirring. The suspension was aged overnight, and then the solid was separated by washing with water and dried at 60°C under vacuum. The obtained sample was labeled as 1.3Ag-ASN.

The Ni²⁺ ions were introduced via complexation with the free amine groups of the silane grafted on the γ -Al₂O₃ fibers. The procedure for introducing Ni²⁺ ions to Ag-ASN samples is as follows: 0.5 g of obtained sample with supported Ag NPs (xAg-ASN, where x denotes the weight percentage of silver in the catalysts) was mixed with 30 mL of Ni(NO₃)₂ aqueous solution (0.017 M) by a shaker for 24 h at room temperature. Then the solid was washed with water 3 times before drying at 60°C under vacuum. The catalysts obtained were labeled as xAg-ASN-Ni²⁺. This procedure immobilizes Ni²⁺ complexes on the sample surfaces, including the narrow gaps between metal NPs, where hot spots are likely to be generated. The γ -Al₂O₃ nanofibers are ~5 nm thick and 100 nm long, which were sintered to form a highly

porous framework of randomly oriented fibers.⁴⁰ The fibers possessed a large specific surface area of $260 \text{ m}^2 \cdot \text{g}^{-1}$, as seen in Table S2 and Figure S2, where most of the surface area was available for grafting of the silane possessing an NH_2 group to form Ni^{2+} complexes and immobilizing plasmonic NPs. Moreover, the cage-like structure (see Figure 1) could confine the NPs formed within the structure and allow reactant molecules to readily diffuse to the Ni^{2+} complex reaction sites in the vicinity of the metal NPs through inter-fiber voids.

Photocatalytic Reactions

The photocatalytic reaction was conducted in a light reaction chamber. A 10 mL Pyrex glass tube was used as the reaction container. After adding the reactants and catalyst, the tube was filled with argon and sealed with a rubber septum cap. Then the tube was placed above a magnetic stirrer with stirring, and illuminated under a halogen lamp (Philips Industries: 500W, wavelength in the range of 400–750 nm). An air conditioner was set to the light reaction chamber to control the reaction temperature. Reactions were also conducted in the dark at the same temperature for comparison. The reaction temperature in the dark was maintained the same as the reaction under irradiation. All the reactions in the dark were conducted using an oil bath placed on a magnetic stirrer. The tube was wrapped with aluminum foil to avoid exposure of the reaction to light. After the reaction, the mixture was collected and filtered through a Millipore filter (pore size $0.45 \mu\text{m}$) to remove the solid photocatalyst. The products were analyzed by an Agilent 6890 gas chromatography (GC) with HP-5 column. An Agilent HP5973 mass spectrometer was used to identify the product. All the products concentrations were calibrated with an external standard method.

Catalyst Characterization

XRD patterns of the samples were recorded on a Philips PANalytical X'Pert PRO diffractometer using $\text{CuK}\alpha$ radiation ($\lambda=1.5418 \text{ \AA}$). The working power was 40 kV and 40 mA. The diffraction data were collected from 10° to 80° with a resolution of 0.01° (2θ). FT-IR measurements were conducted on PerkinElmer Spectrum.² The samples were prepared in KBr pellets and stabilized under controlled relative humidity before acquiring the spectrum. Attenuated total reflectance Fourier transform infrared (ATR-FTIR) spectra were collected by a Nicolet-5700 spectrometer in the wavenumber range between $4,000$ and 620 cm^{-1} at resolution 4 cm^{-1} . The particle size and morphology of the catalyst samples was characterized with a JEOL2100 transmission electron microscope, equipped with a Gatan Orius SC1000 CCD camera. Nitrogen physisorption isotherms were measured at -196°C on the Tristar II 3020. Prior to each measurement, the sample was degassed at 120°C for 24 h under vacuum. The specific surface areas of the samples were calculated by using the Brauner-Emmet-Teller (BET) method and the nitrogen adsorption data in a relative pressure (P/P_0) range between 0.05 and 0.2. Varian Cary 5000 spectrometer was used to collect the data for the diffuse reflectance UV-visible (DR-UV-vis) spectra of the samples. EPR spectra were recorded with a Burkert EPR ELEXSYS 500 spectrometer operating at a frequency of 9.5 GHz in the X-band mode. Metal content in catalysts were obtained by inductively coupled plasma optical emission spectrometry (ICP-OES) carried out on a R4 PerkinElmer ICP-OES 8300DV instrument. Prior to analysis, the powder samples were dissolved in HNO_3 (70%) and diluted by deionized water. Electrochemical measurements were conducted with Bio-Logic SAS potentiostat model VSP. All Raman spectra were taken with a 532 nm excitation laser, 10 s exposure, one-time accumulation, and a Raman imaging setup based on a Renishaw Invia Raman microscope was used.

SUPPLEMENTAL INFORMATION

Supplemental Information can be found online at <https://doi.org/10.1016/j.chempr.2019.07.022>.

ACKNOWLEDGMENTS

We acknowledge financial support from the Australian Research Council (DP150102110). The electron microscopy work was performed through a user project supported by the Central Analytical Research Facility (CARF), Queensland University of Technology.

AUTHOR CONTRIBUTIONS

P.F.H. performed all the experiments. H.Y.Z. and S.S. supervised the project. E.W. and Q.X. provided valuable discussion and revised the manuscript. D.G. provided simulation of EM field. The manuscript was written through contributions of all authors.

DECLARATION OF INTERESTS

The authors declare no competing interests.

Received: March 24, 2019

Revised: June 12, 2019

Accepted: July 25, 2019

Published: August 22, 2019

REFERENCES AND NOTES

- Chen, X., Zhu, H.Y., Zhao, J.C., Zheng, Z.F., and Gao, X.P. (2008). Visible-light-driven oxidation of organic contaminants in air with gold nanoparticle catalysts on oxide supports. *Angew. Chem.* *120*, 5433–5436.
- Zhu, H., Ke, X., Yang, X., Sarina, S., and Liu, H. (2010). Reduction of nitroaromatic compounds on supported gold nanoparticles by visible and ultraviolet light. *Angew. Chem. Int. Ed.* *49*, 9657–9661.
- Christopher, P., Xin, H., and Lincic, S. (2011). Visible-light-enhanced catalytic oxidation reactions on plasmonic silver nanostructures. *Nat. Chem.* *3*, 467–472.
- Lincic, S., Christopher, P., and Ingram, D.B. (2011). Plasmonic-metal nanostructures for efficient conversion of solar to chemical energy. *Nat. Mater.* *10*, 911–921.
- Hu, Y., Liu, Y., Li, Z., and Sun, Y. (2014). Highly asymmetric, interfaced dimers made of Au nanoparticles and bimetallic nanoshells: synthesis and photo-enhanced catalysis. *Adv. Funct. Mater.* *24*, 2828–2836.
- Kale, M.J., Avanesian, T., and Christopher, P. (2014). Direct photocatalysis by plasmonic nanostructures. *ACS Catal.* *4*, 116–128.
- Wang, C., and Astruc, D. (2014). Nanogold plasmonic photocatalysis for organic synthesis and clean energy conversion. *Chem. Soc. Rev.* *43*, 7188–7216.
- Peng, S., McMahon, J.M., Schatz, G.C., Gray, S.K., and Sun, Y. (2010). Reversing the size-dependence of surface plasmon resonances. *Proc. Natl. Acad. Sci. USA* *107*, 14530–14534.
- Lincic, S., Aslam, U., Boerigter, C., and Morabito, M. (2015). Photochemical transformations on plasmonic metal nanoparticles. *Nat. Mater.* *14*, 567–576.
- Zhou, L., Zhang, C., McClain, M.J., Manjavacas, A., Krauter, C.M., Tian, S., Berg, F., Everitt, H.O., Carter, E.A., Nordlander, P., et al. (2016). Aluminum nanocrystals as a plasmonic photocatalyst for hydrogen dissociation. *Nano Lett.* *16*, 1478–1484.
- Smith, J.G., Faucheaux, J.A., and Jain, P.K. (2015). Plasmon resonances for solar energy harvesting: a mechanistic outlook. *Nano Today* *10*, 67–80.
- Zhang, Y., He, S., Guo, W., Hu, Y., Huang, J., Mulcahy, J.R., and Wei, W.D. (2018). Surface-plasmon-driven hot electron photochemistry. *Chem. Rev.* *118*, 2927–2954.
- Huang, Y.F., Zhang, M., Zhao, L.B., Feng, J.M., Wu, D.Y., Ren, B., and Tian, Z.Q. (2014). Activation of oxygen on gold and silver nanoparticles assisted by surface plasmon resonances. *Angew. Chem.* *126*, 2385–2389.
- García, M.A. (2011). Surface plasmons in metallic nanoparticles: fundamentals and applications. *J. Phys. D: Appl. Phys.* *44*, 1–283001.20.
- Sarina, S., Zhu, H., Jaatinen, E., Xiao, Q., Liu, H., Jia, J., Chen, C., and Zhao, J. (2013). Enhancing catalytic performance of palladium in gold and palladium alloy nanoparticles for organic synthesis reactions through visible light irradiation at ambient temperatures. *J. Am. Chem. Soc.* *135*, 5793–5801.
- Dong, Z., Ren, Z., Thompson, S.J., Xu, Y., and Dong, G. (2017). Transition-metal-catalyzed C–H alkylation using alkenes. *Chem. Rev.* *117*, 9333–9403.
- Tasker, S.Z., Standley, E.A., and Jamison, T.F. (2014). Recent advances in homogeneous nickel catalysis. *Nature* *509*, 299–309.
- Hopkinson, M.N., Richter, C., Schedler, M., and Glorius, F. (2014). An overview of N-heterocyclic carbenes. *Nature* *510*, 485–496.
- Kelley, P., Lin, S., Edouard, G., Day, M.W., and Agapie, T. (2012). Nickel-mediated hydrogenolysis of C–O bonds of aryl ethers: what is the source of the hydrogen? *J. Am. Chem. Soc.* *134*, 5480–5483.
- Mulugeta, D., Kim, K.H., Watanabe, K., Menzel, D., and Freund, H.J. (2008). Size effects in thermal and photochemistry of (NO)₂ on Ag nanoparticles. *Phys. Rev. Lett.* *101*, 146103.
- Michaels, A.M., Jiang, J., and Brus, L. (2000). Ag nanocrystal junctions as the site for surface-enhanced Raman scattering of single rhodamine 6G molecules. *J. Phys. Chem. B* *104*, 11965–11971.
- Xu, H., and Käll, M. (2002). Surface-plasmon-enhanced optical forces in silver nanoaggregates. *Phys. Rev. Lett.* *89*, 246802–1–4.
- Twilton, J., Le, C., Zhang, P., Shaw, M.H., Evans, R.W., and Macmillan, D.W.C. (2017). The merger of transition metal and photocatalysis. *Nat. Rev. Chem.* *1*, 0052.1–18.
- Kim, Y., Smith, J.G., and Jain, P.K. (2018). Harvesting multiple electron–hole pairs

- generated through plasmonic excitation of Au nanoparticles. *Nat. Chem.* **10**, 763–769.
25. Sarina, S., Zhu, H.Y., Xiao, Q., Jaatinen, E., Jia, J., Huang, Y., Zheng, Z., and Wu, H. (2014). Viable photocatalysts under solar-spectrum irradiation: nonplasmonic metal nanoparticles. *Angew. Chem.* **53**, 2930–2940.
 26. Zuo, Z., Ahneman, D.T., Chu, L., Terrett, J.A., Doyle, A.G., and MacMillan, D.W. (2014). Merging photoredox with nickel catalysis: coupling of α -carboxyl sp^3 -carbons with aryl halides. *Science* **345**, 437–440.
 27. Tellis, J.C., Primer, D.N., and Molander, G.A. (2014). Dual catalysis. Single-electron transmetalation in organoboron cross-coupling by photoredox/nickel dual catalysis. *Science* **345**, 433–436.
 28. Terrett, J.A., Cuthbertson, J.D., Shurtleff, V.W., and MacMillan, D.W. (2015). Switching on elusive organometallic mechanisms with photoredox catalysis. *Nature* **524**, 330–334.
 29. Tasker, S.Z., and Jamison, T.F. (2015). Highly regioselective indoline synthesis under nickel/photoredox dual catalysis. *J. Am. Chem. Soc.* **137**, 9531–9534.
 30. Sergeev, A.G., and Hartwig, J.F. (2011). Selective, nickel-catalyzed hydrogenolysis of aryl ethers. *Science* **332**, 439–443.
 31. He, J., Zhao, C., and Lercher, J.A. (2012). Ni-catalyzed cleavage of aryl ethers in the aqueous phase. *J. Am. Chem. Soc.* **134**, 20768–20775.
 32. Sergeev, A.G., Webb, J.D., and Hartwig, J.F. (2012). A heterogeneous nickel catalyst for the hydrogenolysis of aryl ethers without arene hydrogenation. *J. Am. Chem. Soc.* **134**, 20226–20229.
 33. Wang, X., and Rinaldi, R. (2013). A route for lignin and bio-oil conversion: dehydroxylation of phenols into arenes by catalytic tandem reactions. *Angew. Chem. Int. Ed. Engl.* **52**, 11499–11503.
 34. Wang, X., and Rinaldi, R. (2012). Exploiting H-transfer reactions with RANEY®Ni for upgrade of phenolic and aromatic biorefinery feeds under unusual, low-severity conditions. *Energy Environ. Sci.* **5**, 8244–8260.
 35. Molinari, V., Giordano, C., Antonietti, M., and Esposito, D. (2014). Titanium nitride-nickel nanocomposite as heterogeneous catalyst for the hydrogenolysis of aryl ethers. *J. Am. Chem. Soc.* **136**, 1758–1761.
 36. Zeng, H., Cao, D., Qiu, Z., and Li, C.J. (2018). Palladium-catalyzed formal cross-coupling of diaryl ethers with amines: slicing the 4-O-5 linkage in lignin models. *Angew. Chem. Int. Ed.* **57**, 3814–3819.
 37. Deuss, P.J., and Barta, K. (2016). From models to lignin: transition metal catalysis for selective bond cleavage reactions. *Coord. Chem. Rev.* **306**, 510–532.
 38. Nguyen, J.D., Matsuura, B.S., and Stephenson, C.R. (2014). A photochemical strategy for lignin degradation at room temperature. *J. Am. Chem. Soc.* **136**, 1218–1221.
 39. Zakzeski, J., Bruijninx, P.C., Jongerius, A.L., and Weckhuysen, B.M. (2010). The catalytic valorization of lignin for the production of renewable chemicals. *Chem. Rev.* **110**, 3552–3599.
 40. Yang, D., Paul, B., Xu, W., Yuan, Y., Liu, E., Ke, X., Wellard, R.M., Guo, C., Xu, Y., Sun, Y.H., et al. (2010). Alumina nanofibers grafted with functional groups: a new design in efficient sorbents for removal of toxic contaminants from water. *Water Res.* **44**, 741–750.
 41. Park, D.H., Park, S.S., and Choe, S.J. (1999). The formation of metal (M = Co (II), Ni (II), and Cu (II)) complexes by aminosilanes immobilized within mesoporous molecular sieves. *Bull. Korean Chem. Soc.* **20**, 291–296.
 42. Khatib, A., Aqra, F., Deamer, D., and Oliver, A. (2009). Crystal structure of [bis (l-alaninato) diaqua] nickel (II) dihydrate. *Int. J. Inorg. Chem.* **2009**, 1–5.
 43. Link, S., and El-Sayed, M.A. (1999). Substrates matter: influence of an adjacent dielectric on an individual plasmonic nanoparticle. *J. Phys. Chem. B* **103**, 4212–4217.
 44. Knight, M.W., Wu, Y., Lassiter, J.B., Nordlander, P., and Halas, N.J. (2009). Substrates matter: influence of an adjacent dielectric on an individual plasmonic nanoparticle. *Nano Lett.* **9**, 2188–2192.
 45. Kamat, P.V. (2002). Photophysical, photochemical and photocatalytic aspects of metal nanoparticles. *J. Phys. Chem. B* **106**, 7729–7744.
 46. Wei, H., and Xu, H. (2013). Hot spots in different metal nanostructures for plasmon-enhanced Raman spectroscopy. *Nanoscale* **5**, 10794–10805.
 47. Davis, T.J., and Gómez, D.E. (2017). Colloquium: an algebraic model of localized surface plasmons and their interactions. *Rev. Mod. Phys.* **89**, 011003–1–20.
 48. Stockman, M.I., Shalaev, V.M., Moskovits, M., Botet, R., and George, T.F. (1992). Enhanced Raman scattering by fractal clusters: scale-invariant theory. *Phys. Rev. B* **46**, 2821–2830.
 49. Ding, S.Y., You, E.M., Tian, Z.Q., and Moskovits, M. (2017). Electromagnetic theories of surface-enhanced Raman spectroscopy. *Chem. Soc. Rev.* **46**, 4042–4076.
 50. Camden, J.P., Dieringer, J.A., Wang, Y., Masiello, D.J., Marks, L.D., Schatz, G.C., and Van Duyne, R.P. (2008). Probing the structure of single-molecule surface-enhanced Raman scattering hot spots. *J. Am. Chem. Soc.* **130**, 12616–12617.
 51. Sarina, S., Peiris, E., Waclawik, E.R., Ayoko, G.A., Han, P., Jia, J., and Zhu, H.Y. (2019). Plasmonic switching of reaction pathway: visible-light irradiation varies reactant concentration at the solid-solution interface of a gold-cobalt catalyst. *Angew. Chem.* <https://doi.org/10.1002/ange.201904452>.
 52. Sarina, S., Jaatinen, E., Xiao, Q., Huang, Y.M., Christopher, P., Zhao, J.C., and Zhu, H.Y. (2017). Photon energy threshold in direct photocatalysis with metal nanoparticles: key evidence from the action spectrum of the reaction. *J. Phys. Chem. Lett.* **8**, 2526–2534.
 53. Carpenter, M.K., and Corrigan, D.A. (1989). Photoelectrochemistry of nickel hydroxide thin films. *J. Electrochem. Soc.* **136**, 1022–1026.
 54. Aslam, U., Rao, V.G., Chavez, S., and Lincic, S. (2018). Catalytic conversion of solar to chemical energy on plasmonic metal nanostructures. *Nat. Catal.* **1**, 656–665.
 55. Alabastri, A., Yang, X., Manjavacas, A., Everitt, H.O., and Nordlander, P. (2016). Extraordinary light-induced local angular momentum near metallic nanoparticles. *ACS Nano* **10**, 4835–4846.
 56. Singh, V., Srinivas, V., and Ram, S. (2010). Structural and magnetic properties of polymer-stabilized tetragonal Ni nanoparticles. *Philos. Mag.* **90**, 1401–1414.
 57. Otto, A., Mrozek, I., Grabhorn, H., and Akemann, W. (1992). Surface-enhanced Raman scattering. *J. Phys.: Condens. Matter* **4**, 1143–1212.
 58. Edouard, G.A., Kelley, P., Herbert, D.E., and Agapie, T. (2015). Aryl ether cleavage by group 9 and 10 transition metals: stoichiometric studies of selectivity and mechanism. *Organometallics* **34**, 5254–5277.
 59. Zhu, H.Y., Riches, J.D., and Barry, J.C. (2002). γ -alumina nanofibers prepared from aluminum hydrate with poly (ethylene oxide) surfactant. *Chem. Mater.* **14**, 2086–2093.